RSC Advances

PAPER

View Article Online
View Journal | View Issue

Cite this: *RSC Adv.*, 2025, **15**, 49063

Light trapping and guided mode enhancement in perovskite/Si tandem solar cells with embedded silicon nanowires

Arpan Saha, †[a] Mohammad Ajmain Fatin, †[a] Tasmiat Rahman [b] and Mainul Hossain *[a]

Energy loss at the interface between the subcells limits the efficiency of existing tandem solar cells. In this work, we propose a novel two-terminal perovskite/silicon tandem solar cell with vertically aligned silicon (Si) nanowires (NWs) incorporated between the two subcells. The sub-wavelength dimensions of the embedded Si NWs, grown on top of the Si bottom subcell, allow efficient light trapping and lead to guided resonant modes. Finite-difference time-domain (FDTD) analysis shows that, across the entire spectrum, these guided modes effectively couple the incident light between the subcells, reducing reflection losses in the interlayer and enhancing absorption in the underlying bottom c-Si cell. To evaluate the performance of the proposed tandem solar cell, we performed electrical simulations using the enhanced carrier generation profile obtained from the FDTD simulations. The proposed embedded NW tandem configuration yields 22.6% enhancement in short-circuit current density compared to conventional architectures, boosting the power conversion efficiency from 26.98% to 32.11%. These findings offer the necessary theoretical framework for experimentalists, providing a clear pathway towards realizing high-performance perovskite/Si tandem solar cells.

Received 30th September 2025
Accepted 2nd December 2025

DOI: 10.1039/d5ra07413d

rsc.li/rsc-advances

1. Introduction

Crystalline silicon (c-Si) has dominated the photovoltaics (PV) market for an extensive period due to well-established processes that yield low-cost and highly stable solar cells with excellent power conversion efficiencies (PCEs). In recent years, perovskite solar cells have attracted a great deal of attention as a promising alternative to c-Si, due to their tunable bandgaps, high absorption coefficients, simpler manufacturing processes, higher PCEs and longer electron and hole diffusion lengths to minimize recombination losses.[1,2] However, the performance of both single junction perovskite and Si cells are limited by the Shockley–Queisser (S–Q) limit.[3] To surpass the S–Q limit, a standalone wide bandgap top perovskite solar cell is stacked with a standalone bottom Si solar cell having a narrower bandgap to form a tandem solar cell. The high energy photons from the incident sunlight are absorbed by the top subcell while the bottom subcell absorbs the low energy photons that pass through the top subcell. This allows absorption over a wider spectral range and hence boosts the PCE of the tandem solar cell.[4,5] Despite the merits, reflection and recombination losses and poor light trapping at the interface between the two subcells degrade tandem solar cell performance. Some attempts to reduce the interlayer losses include the use of spectrally selective interlayers in the perovskite/Si tandems[6] and the mechanical bonding of the subcells through a low-index epoxy as in III–V tandems.[7] Monolithic 2-terminal perovskite/Si tandem solar cells have benefited from the integration of sub-micrometer scale sinusoidal nanotextures at the front surface of the Si subcell, achieving certified PCE as high as 29.8%.[8] For instance, growing III–V nanowires (NWs) on top of Si substrates have enabled multi-junction solar cells with high efficiency when the subcell currents are matched.[8,9] The subwavelength dimensions and high refractive indices of the NWs offer highly efficient broadband light absorption through an optical antenna effect.[10] Finite-difference time-domain (FDTD) analysis confirmed that the one-dimensional (1D) NWs enhance absorption by not only coupling the incident light into guided modes but also by efficiently transporting the sub-bandgap photons to the Si bottom cell.[11] However, Si NWs suffer from indirect bandgap and low absorption coefficient of Si in the 600–1100 nm spectral range. The absorption and conversion efficiency in the visible range can be significantly improved by introducing perovskites, with a direct bandgap and a large absorption coefficient, into the Si NW array.[12] Recent studies have reported the integration of perovskites with Si NW arrays for enhanced broadband absorption in hybrid photodetectors and solar cells. Asuo *et al.* successfully fabricated a hybrid photodetector that combined

[a]*Department of Electrical and Electronic Engineering, University of Dhaka, Dhaka-1000, Bangladesh. E-mail: mainul.eee@du.ac.bd*

[b]*Department of Electronics and Computer Science, University of Southampton, Southampton SO17 1BJ, UK*

† These authors contributed equally.

halide perovskite with vertically aligned Si NW arrays, exhibiting strong broadband absorption for wavelengths ranging from near ultraviolet to near-infrared.[13] Yan *et al.* used technology computer-aided design (TCAD) simulations to evaluate the performance of a Si NW array/perovskite structure. The incorporation of a halide perovskite among the intrinsic regions of a vertically aligned Si axial p–i–n NW array significantly improved the performance of the resulting solar cell, absorbing light between 300–800 nm wavelengths and reaching a PCE as high as 13.3%.[12]

In this paper, we propose a two-terminal (2-T) perovskite/Si tandem solar cell where an array of vertically aligned Si NWs is grown on top of a crystalline-Si (c-Si) bottom subcell. A 50 nm thick layer of indium tin oxide (ITO) is deposited on top of Si NWs, followed by encapsulation with polydimethylsiloxane (PDMS). The height, period, diameter and geometry of the Si NWs can be optimized to maximize absorption in the bottom Si subcell. To demonstrate efficient light coupling by the NWs, FDTD simulations were carried out to investigate the power absorption profile and electric field pattern in the underlying bulk Si. Finally, the output characteristics of the proposed tandem solar cell is benchmarked against a conventional tandem architecture.

2. Device structure and simulation methodology

Fig. 1(a) shows the three-dimensional (3D) schematic of a conventional perovskite/Si tandem solar cell. The proposed device, shown in Fig. 1(b), consists of Si NWs in the interlayer between the two subcells. In each case, the tandem cell is irradiated from the top with AM1.5G, 1 sun spectrum. The vertically aligned Si NW/ITO core shells are grown on top of the 180 μm thick bulk c-Si, which serves as the bottom subcell of the tandem. A layer of PDMS is deposited around the Si NW/ITO core shell array. The ITO layer serves as the recombination junction between the perovskite and the c-Si subcells, confining all electronic transport and recombination beneath it. Since PDMS is deposited only after the ITO junction and lies entirely outside the electronically active layers, it does not affect vertical carrier transport or recombination. Its low refractive index is not detrimental, as PDMS is highly transparent and contributes negligible parasitic absorption; optical behavior is instead governed by the Si-NW/ITO geometry.[14] PDMS primarily provides mechanical stabilization and environmental protection. High-aspect-ratio Si NWs are susceptible to bending or collapse during processing, and PDMS is well established as a conformal, transparent encapsulant that supports NW structures while preserving their optical performance. For instance, Fedorov *et al.*[15] demonstrated gallium phosphide (GaP) NWs embedded within a PDMS membrane, where PDMS serves as a transparent, flexible, and chemically robust framework that preserves the NW morphology and protects the structures during optical operation. For the top perovskite subcell, an experimentally validated n–i–p wide-bandgap perovskite configuration is adopted. Cesium formamidinium lead iodide bromide [$Cs_{0.18}FA_{0.82}Pb(I,Br)_3$] is chosen as the main absorber layer. This mixed halide perovskite has an optical bandgap of ~1.70 eV which ensures strong visible-light absorption and appropriate current matching with the bottom c-Si sub cell. Furthermore, this wide-bandgap composition is also known to exhibit enhanced phase stability and reduced halide segregation under illumination, making it suitable for reliable tandem operation.[16]

The choice of carrier transport layers is also paramount for perovskite solar cell performance. Consequently, significant research efforts are being dedicated to designing robust, cost-effective, and efficient electron and hole transport layers (ETLs and HTLs). A major focus has been replacing the conventional but unstable and expensive HTL, spiro-OMeTAD. Promising alternative strategies include the development of inorganic nanoparticles,[17,18] ionic liquids,[19] dopant-free small molecules,[20] and engineered metallophthalocyanines.[21] These

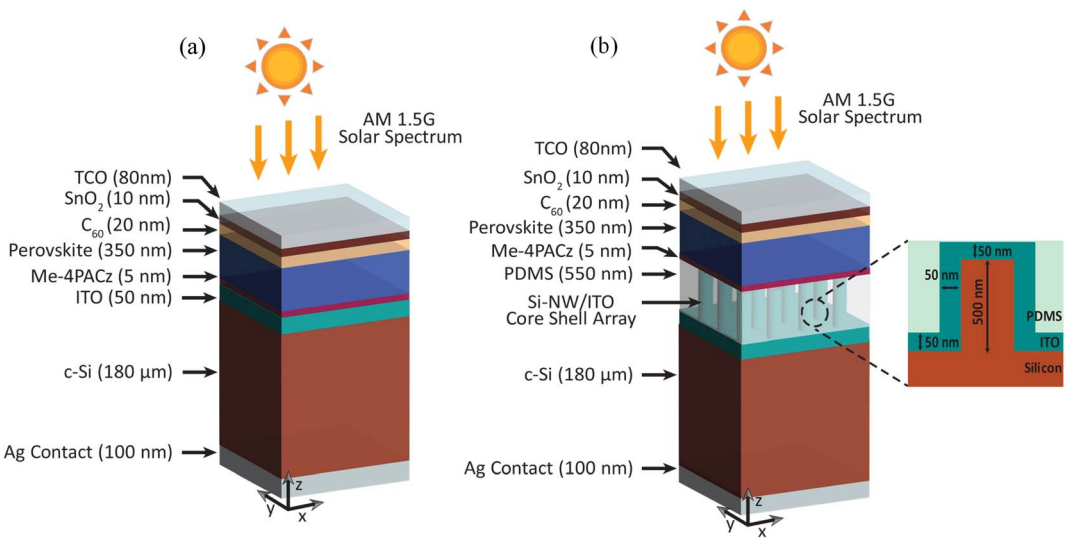

Fig. 1 3D schematic of (a) planar two-terminal perovskite/Si tandem solar cell (b) proposed two-terminal perovskite/Si NW tandem solar cell with Si NW array embedded in the interlayer between the top and the bottom subcells. An enlarged version of a single Si NW surrounded by ITO and PDMS is shown with dimensions optimized for maximum absorption.

next-generation materials aim to provide superior durability and cost-effectiveness while enhancing both power conversion efficiency and long-term stability against environmental stressors like moisture and heat. Here, [4-(3,6-dimethyl-9*H*-carbazol-9-yl)butyl]phosphonic acid (Me-4PACz)—a self-assembled monolayer—is employed as the HTL. Me-4PACz is widely recognized for providing excellent band alignment, effective interfacial passivation, and efficient hole extraction in high-performance perovskite devices. Electron transport is facilitated by a C_{60}/SnO_2 bilayer ETL, where C_{60} acts as the primary electron-transport layer and the SnO_2 overlayer forms a transparent, low-loss electron-selective contact that suppresses interfacial recombination and improves charge-collection stability. This $C_{60}/SnO_2/Cs_{0.18}FA_{0.82}Pb(I,Br)_3$/Me-4PACz stack reflects the transport-layer architecture used in experimentally demonstrated wide-bandgap perovskite/Si tandem solar cells, ensuring that our simulations correspond to a practical and fabrication-feasible device configuration.[16,22]

To validate the simulation framework, the electrical performance of the standalone top and the bottom subcells was simulated using one-dimensional solar cell capacitance simulator (SCAPS-1D), which solves the coupled Poisson, transport, and continuity equations.[23] All simulations were conducted at 300 K. The simulation results were benchmarked against experimentally reported device data under standard AM1.5G, 1-sun illumination.[16] The simulated current density–voltage (J–V) curves (Fig. S1, SI) of the subcells exhibit close agreement with the corresponding experimental results (Table S1, SI), indicating that the optical and electrical models are accurately represented. This validation confirms that the calibrated subcells can be reliably used as the foundation for modeling the complete tandem device.

The optical simulations in this study were carried out using the finite-difference time-domain (FDTD) method which computes the electric and magnetic fields throughout the tandem solar cell by solving Maxwell's equations at every point in space and time. *A* plane wave source, with wavelengths ranging from $\lambda = 300$ nm to 1200 nm, illuminates the tandem cell from the top at normal incidence. The two-dimensional (2D) periodic structure of the Si NWs is in a square array and has a fourfold rotational symmetry about the propagation axis of light. Hence, both the transverse-electric (TE) and the transverse-magnetic (TM) polarizations yield the same absorption spectra when illuminated at normal incidence.[24] Although polarization-dependent effects may emerge at different incident angles, a detailed angle-resolved analysis requires extensive optical modeling which lies outside the scope of the present study. Therefore, all FDTD simulations, in this work, are carried out with the TM waves alone, setting all polarization angles to 0°. Periodic boundary conditions were applied in the x and y directions which allows the periodic array to be modeled by carrying out simulations within the unit cell. Any reflected and transmitted fields were absorbed by applying perfectly matched layer (PML) boundary conditions on the top and the bottom surfaces along the z direction. A frequency domain monitor is placed at the top of the cell to calculate the reflectance $R(\lambda)$ of the simulated structure. The absorbance, $A(\lambda)$, of the tandem was calculated using the equation:

$$A(\lambda) = 1 - R(\lambda) \quad (1)$$

assuming that no light is transmitted once it passes the semi-infinite silicon bulk layer.

The two-dimensional (2D) frequency domain field and power monitors, placed within the unit cell, are used to compute the electric field and power absorption profiles. The absorbed power (P_{abs}) per unit volume, electric field (E) and the permittivity (ε) of the medium, are all functions of position (r) and wavelength (λ) and can be expressed as:[25]

$$P_{abs} = -\frac{1}{2}\omega|E(\mathrm{r},\lambda)|^2 I_m[\varepsilon(r,\lambda)] \quad (2)$$

P_{abs} is normalized by dividing by the incident power at each wavelength. Assuming every photon absorbed yields one electron–hole pair, the carrier generation rate per unit volume ($G(\mathrm{r})$) can be expressed as:[25]

$$G(r) = \int \frac{P_{abs}}{hc}\lambda \mathrm{d}\lambda \quad (3)$$

where h is Planck's constant and c is the speed of light in vacuum.

The dimensions of the Si NWs in the interlayer were optimized to maximize light absorption across the target spectral range. This is achieved by evaluating the absorption spectra obtained from the FDTD simulations at different NW radius (r_{nw}) and period (P) while keeping the NW height fixed at 500 nm. Results show that the $r_{nw} = 250$ nm and $P = 700$ nm (Fig. S2, SI) yield the maximum absorption. Although increasing NW height can further strengthen light trapping and mode confinement, excessively tall NWs often suffer from mechanical instability caused by capillary forces during wet processing or stress arising from subsequent layer deposition.[23,24] For this reason, the NW height was limited to 500 nm—chosen as a practical cutoff that balances optical enhancement with structural robustness. Fig. 1(b) shows an enlarged version of a single Si NW, surrounded by ITO and PDMS, with dimensions optimized for maximum absorption.

Finally, the optical generation profile from FDTD simulations was incorporated in SCAPS-1D to evaluate the current–voltage characteristics of the tandem solar cell. Device efficiency was further optimized through a current-matching approach by adjusting absorber thicknesses to match the subcell currents. All input parameters, including the interface defect densities, used in the electrical simulations were taken from well-established literature sources reporting standard and experimentally validated values (Tables S2 and S3, SI).

3. Proposed fabrication scheme

Several methods have been adopted in the past to fabricate vertically aligned Si NW arrays. These include bottom-up techniques like vapor–liquid-solid (VLS)[26] and supercritical fluid–liquid–solid (SFLS)[27] mechanisms as well as more controllable top-down approaches like the metal-assisted chemical etching (MACE).[28] The Si NWs proposed in our study can be fabricated using the combination of cryogenic inductively coupled plasma reactive ion

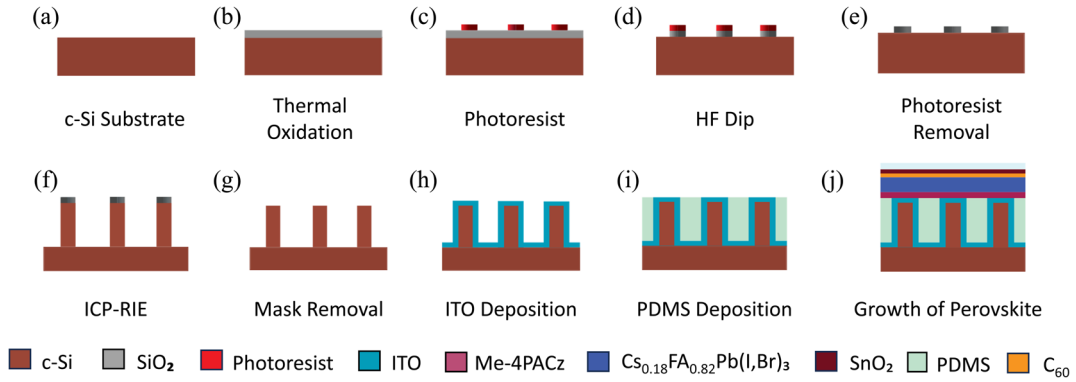

Fig. 2 Fabrication scheme of the proposed perovskite/Si solar cell with vertically aligned Si NWs grown on top of the c-Si bottom cell. (a) c-Si substrate (b) wet thermal oxidation SiO_2 (c) patterning using standard photolithography process (d) dipping into hydrofluoric acid (HF) solution to transfer the pattern (e) removal of photoresist using acetone (f) cryogenic dry etching of the patterned Si with inductively coupled plasma reactive ion etching (ICP-RIE) process to form the vertically aligned Si NWs (g) removal of photoresist masks (h) deposition of indium tin oxide (ITO) core shell using MOCVD (i) spin-coating of PDMS layer (j) deposition of HTL, perovskite and ETL.

etching (ICP-RIE) and photolithography as shown in Fig. 2. This method, demonstrated by Refino *et al.*[29] yields doping independent, high aspect-ratio, vertically aligned Si NWs with smooth side walls and a homogeneous geometry. The c-Si substrate can be patterned using photolithography and then etched using plasma containing ions and radicals. Once the NWs are formed, a 50 nm thin layer of indium tin-oxide (ITO) can be deposited on top by horizontal-type MOCVD forming a core–shell structure. Pal *et al.* reported a similar In *P*–SiNW core–shell structure using MOCVD at atmospheric pressure.[30] After the deposition of ITO, a PDMS layer can be deposited on top of the ITO-coated Si-NW array using a two-step spin coating process. In the first step, the PDMS uniformly fills up the dense Si-NW array. The excess residue of the PDMS on top of the array can be removed in the second step of the spin coating process which gives it a uniform planar configuration.[31] After depositing the ITO shell, a Me-4PACz self-assembled monolayer is first spin-coated onto the ITO-coated Si NWs to form the hole-selective contact. The perovskite absorber is then deposited using a one-step spin-coating method followed by thermal annealing. A compact C_{60} electron-transport layer is subsequently added *via* thermal evaporation, and finally, a conformal SnO_2 layer is deposited using low-temperature ALD to complete the device stack.[16]

4. Results and discussion

Fig. 3(a) compares the average absorption (A_{avg}) between the standalone perovskite solar cell (top subcell), a standalone c-Si solar cell with Si NW array (bottom subcell), a conventional perovskite/Si tandem solar cell and the proposed perovskite/Si NW solar cell with vertically aligned Si NWs grown on top of the bulk Si. The average absorption is defined as:[32]

$$A_{avg} = \frac{1}{\lambda_{max} - \lambda_{min}} \int_{\lambda_{min}}^{\lambda_{max}} A(\lambda) d\lambda \quad (4)$$

The corresponding absorbed spectral irradiance under AM 1.5G for the different solar cells are illustrated in Fig. 3(b). Compared to conventional perovskite/Si tandem solar cells, the proposed tandem design, with vertically aligned Si NWs in the

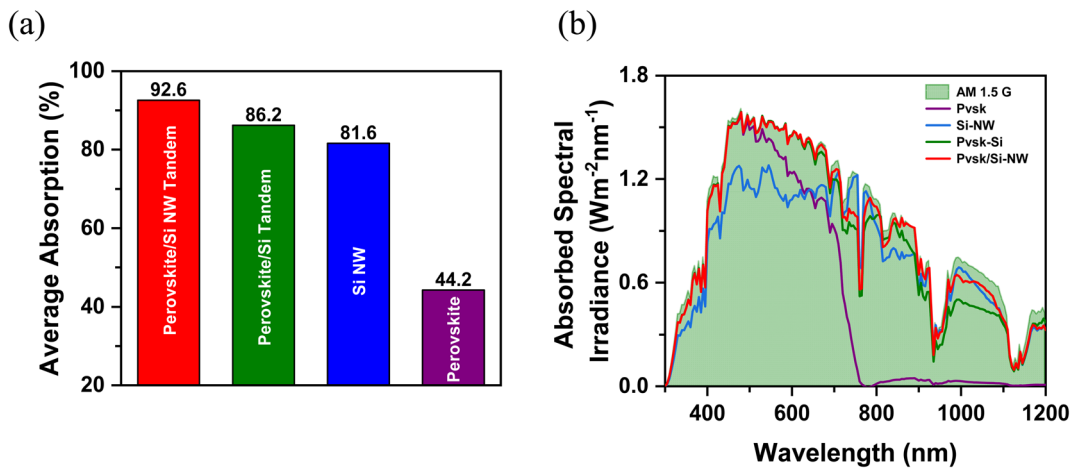

Fig. 3 (a) Average absorption and (b) absorbed spectral irradiance under AM 1.5G of a standalone perovskite, a standalone Si NW array, a planar perovskite/Si tandem and a perovskite/Si NW solar cell over the entire spectral range.

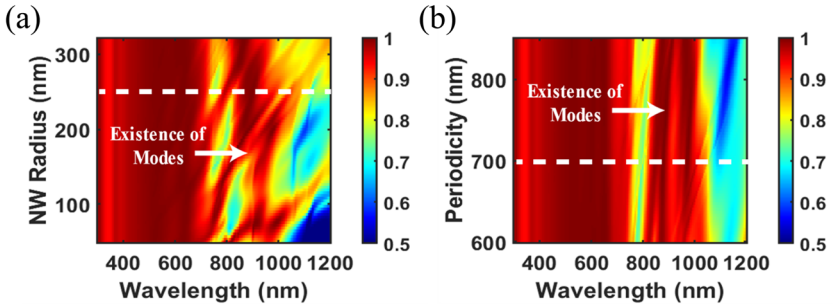

Fig. 4 Contour plot of absorption as a function of the wavelength of incident light and (a) NW radius, (b) NW period in a perovskite/Si NW tandem. The dash-dotted white line represents NW with $r_{NW} = 250$ nm and $P = 700$ nm. The NW height is fixed at 500 nm.

interlayer, clearly shows enhanced absorption of the AM 1.5G spectrum, leading to an average absorption, A_{avg}, as high as 92.6%. A standalone c-Si NW array exhibits superior absorption enhancement in the near infrared (NIR) region. Therefore, the integration of a top perovskite absorber layer with the light trapping and scattering capabilities of the Si NW array results in a highly efficient broadband absorber, outperforming other examined structures. The results are consistent with the previous study by Garnett *et al.* which demonstrated that ordered arrays of Si NWs can increase the path length of incident light by up to a factor of ~73, enabling superior light-trapping and increased absorption over the entire AM1.5 G spectrum.[33] The strong interaction between the incident light and the sub-wavelength Si NWs gives rise to a variety of optical effects that include wave-guiding, Fabry–Pérot resonances, low reflectivity (moth-eye effect), diffractive effects and near-field coupling.[34] These effects are highly tunable by adjusting the NW array geometry and provide precise control on the reflection, absorption, and scattering properties of light for enhanced absorption.

4.1 Waveguiding effect

The vertically aligned Si NWs can act as subwavelength dielectric cylindrical waveguides that can efficiently couple incident light, parallel to its long axis, into leaky resonant modes. Earlier, simulations by Wang *et al.*[35] have shown that the incident waves can only couple to HE_{1m} leaky modes, where 1 is the azimuthal mode number and m the radial mode number, which represents the radial variation of the electromagnetic field. The strength of the coupled modes depends on the wavelength of the incident light and can be tuned across the entire spectrum by simply varying the radius of the NW.

Fig. 4(a) shows a contour plot of the simulated absorption characteristics of the proposed tandem as a function of wavelength of incident light and the NW radius. The colored bands correspond to guided mode resonances, where incident light is efficiently coupled into the NW array. The transverse leaky mode resonances, associated with the fundamental HE_{11} mode, are responsible for the broader red bands, where partial confinement of light enhances the field intensity before radiating into free space. With the increasing NW radii, the resonant modes are red shifted towards longer wavelengths. Also, NWs with larger radii (r_{NW}) can sustain multiple modes. Due to the symmetric nature of the NWs and their longer dimensions, the interactions with the higher guided modes, and consequently the absorption enhancements, are much weaker. Hence, only the coupling of the fundamental HE_{11} mode primarily contributes to the absorption enhancement. For $r_{NW} > 250$ nm, longitudinal resonant modes appear for $\lambda > 800$ nm. These are weaker than the transverse modes, but can couple to them, giving rise to interference between the modal fields at longer wavelengths. Fig. 4(b) shows the variation of wavelength-dependent absorption characteristics with NW period. The white dashed line indicates the NW radius (Fig. 4(a)) and period (Fig. 4(b)) selected for the proposed structure. The chosen radius and period support multiple guided and leaky mode resonances across visible and near-infrared regions, ensuring efficient coupling of incident light into the underlying Si and is responsible for the enhanced broadband absorption.[11,34–36] The NW array leverages the entire spectrum of incident light without requiring additional light-trapping techniques such as surface texturing. Moreover, the unique geometry of Si NWs permit increased optical path lengths and reduced reflections at the perovskite/Si interface.[37,38] The scattering and coupling of light between adjacent Si NWs increase the absorption further by causing multiple interactions with the Si bottom cell. Also, the NWs restrict a sharp change in refractive index by providing gradual transition in the refractive index, leading to reduced reflection losses.[39]

To elucidate the near-field coupling of incident light into the underlying c-Si absorber, the spatial distributions of the absorbed power density in the z–x plane, extracted from power monitors at $\lambda = 616$ nm, 879 nm, and 965 nm, are presented in Fig. 5(a), (c), and (e) for the Si NWs on c-Si. The corresponding absorption distributions for the planar c-Si reference are shown in Fig. 5(b), (d), and (f), respectively. At each wavelength, the transmitted power through the monitors is normalized to the maximum absorption obtained across both configurations. At shorter wavelengths (*e.g.*, 616 nm), where the photon energy exceeds the perovskite bandgap, absorption predominantly occurs within the perovskite top cell, leading to negligible coupling into the bottom c-Si layer. In contrast, at longer wavelengths (879 nm and 965 nm), which lie below the perovskite absorption edge, the incident light couples strongly into the Si NW and the underlying c-Si. Hence, for the NW

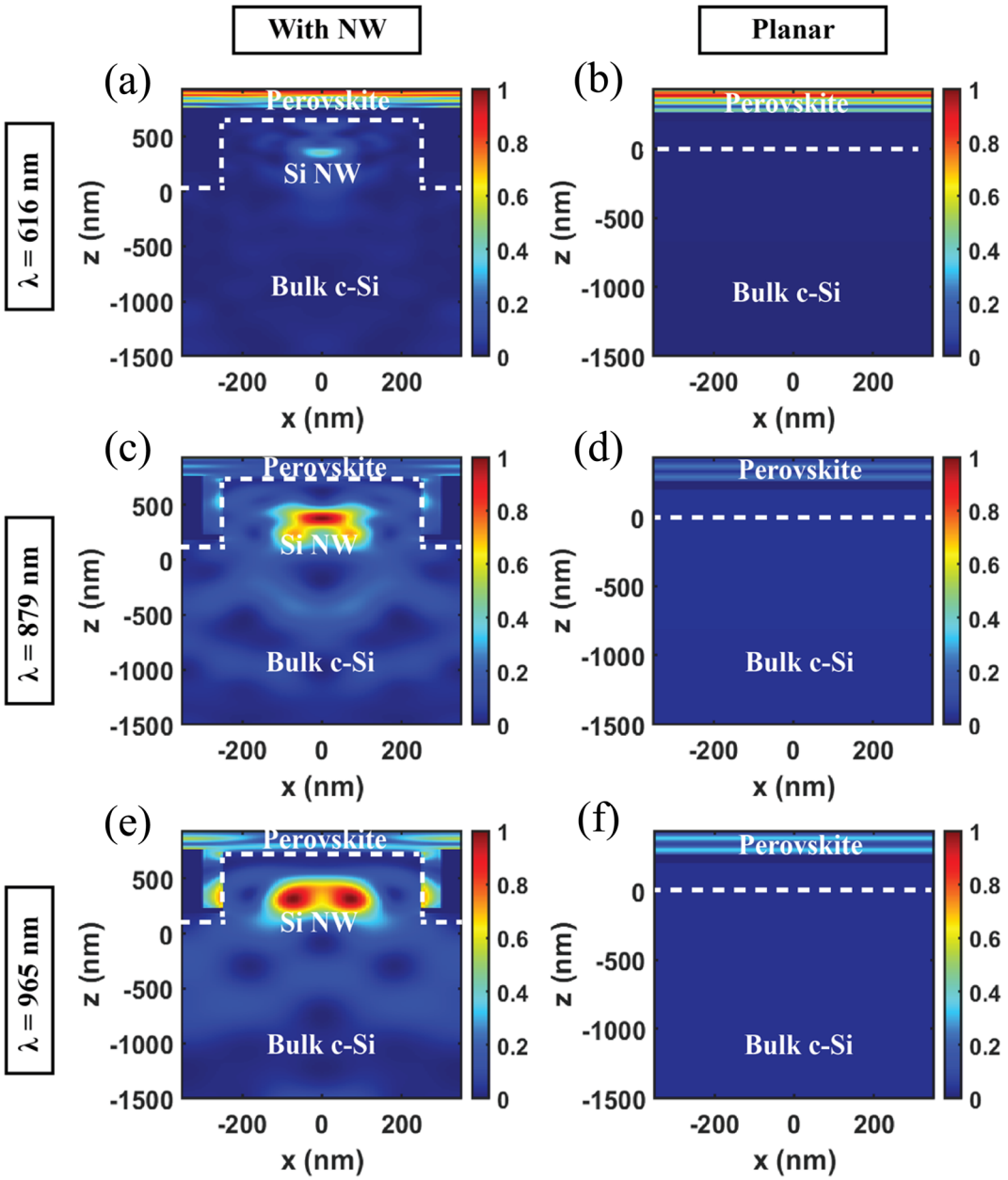

Fig. 5 Normalized magnitude of the power absorption at $\lambda = 616$ nm, 879 nm, 965 nm for perovskite/Si NW tandem solar cell [(a), (c) and (e)] and perovskite/Si tandem cell [(b), (d) and (f)].

configuration, pronounced absorption occurs not only within the Si NWs themselves but also in the underlying bulk, facilitated by enhanced scattering and redistribution of the incident field. This effect yields a substantially higher absorption compared to planar c-Si, further highlighting the role of NW geometry in facilitating light harvesting. Importantly, for planar c-Si, the simulations confirm negligible near-field coupling, with the incident light largely transmitted or reflected, resulting in minimal electric field penetration into the c-Si substrate. By contrast, the Si NW array introduces strong localized field enhancements and act as scattering centers that redirect and couple the incident light into the bottom Si subcell.

4.2 Fabry–Pérot resonance

Vertically aligned Si NWs, when illuminated along their long axis under normal incidence, can sustain Fabry–Pérot resonance modes. This effect is also observed in our proposed structure, as illustrated by the electric field distribution at $\lambda = 990$ nm in Fig. 6(b), confirming the presence of standing wave patterns indicative of Fabry–Pérot resonances. The nodes of the electric field are seen to be evenly spaced along the NW long-axis. Fabry–Pérot resonance occurs when the incident light reflects off both the top and bottom of the NW array, creating a standing wave that results in a distinct dip in the reflectance spectrum, as shown in Fig. 6(a). Formation of Fabry–Pérot cavities require the roundtrip

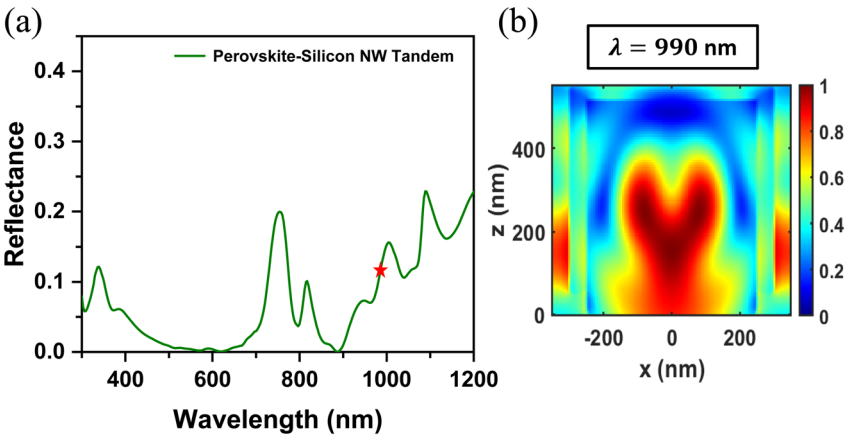

Fig. 6 (a) Reflectance spectrum of the perovskite/Si NW tandem showing oscillations resulting from Fabry–Pérot resonances in the NW array (b) corresponding normalized magnitude of the electric field surrounding the NW at $\lambda = 990$ nm (marked with an asterisk in (a)).

NW length (2h) to be an integer (m) multiple of the effective wavelength (λ_{eff}) of the NW guided mode such that $2h = m \times \lambda_{eff}$, where $\lambda_{eff} = \lambda_o/n_{eff}$ with λ_o as the effective wavelength in the NW and n_{eff} as the effective refractive index. For our proposed NW array, this condition is fulfilled at multiple wavelengths, giving rise to oscillations in the reflectance spectrum of Fig. 6(a). Provided that the NWs are closely packed, Fabry–Pérot resonance can confine light in the gaps between the NWs.[34,40] This can couple incident light into the bulk substrate as the substrate refractive index decreases. Given that the refractive index of Si decreases with increasing wavelength above the bandgap, the characteristic dips in the reflection spectrum also increases with increasing wavelength.[36] The contribution of these effects to the overall absorption enhancement can be further evaluated by calculating the ratio of absorption within NWs to bulk Si absorption at specific wavelengths (Fig. S3, SI).

4.3 Optical carrier generation rate

Fig. 7(a) illustrates the carrier generation rate inside the bulk c-Si layer, as a function of the c-Si thickness, with and without the

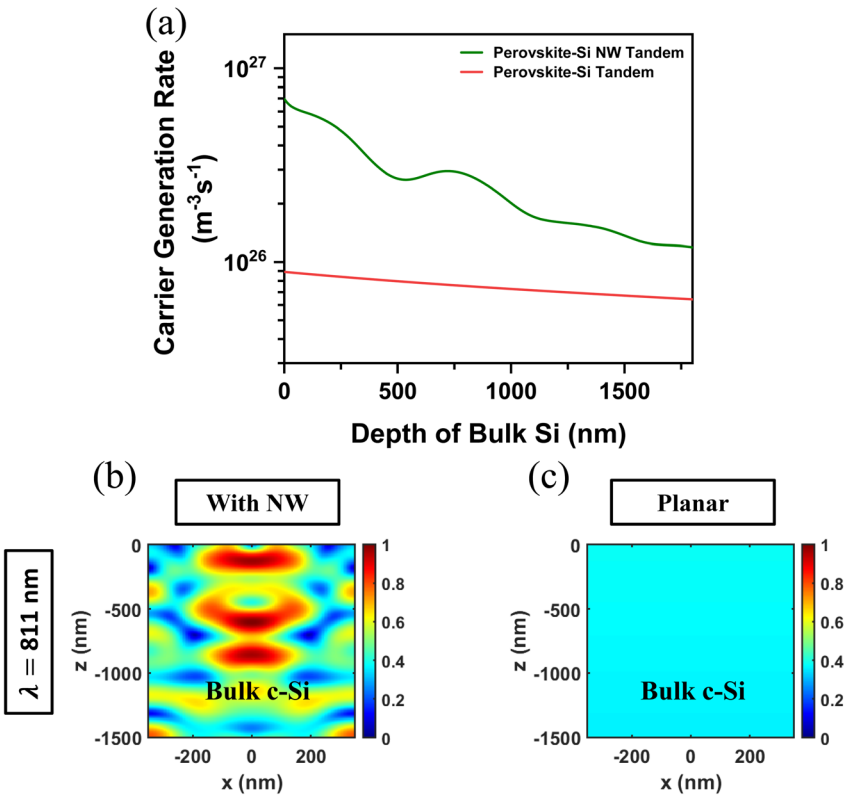

Fig. 7 (a) Carrier generation rate within bulk c-Si as a function of Si depth for both perovskite/Si tandem and perovskite/Si NW tandem solar cells. Electric-field profile inside bulk c-Si at $\lambda = 811$ nm (b) with Si NW array on top (c) without Si NW array.

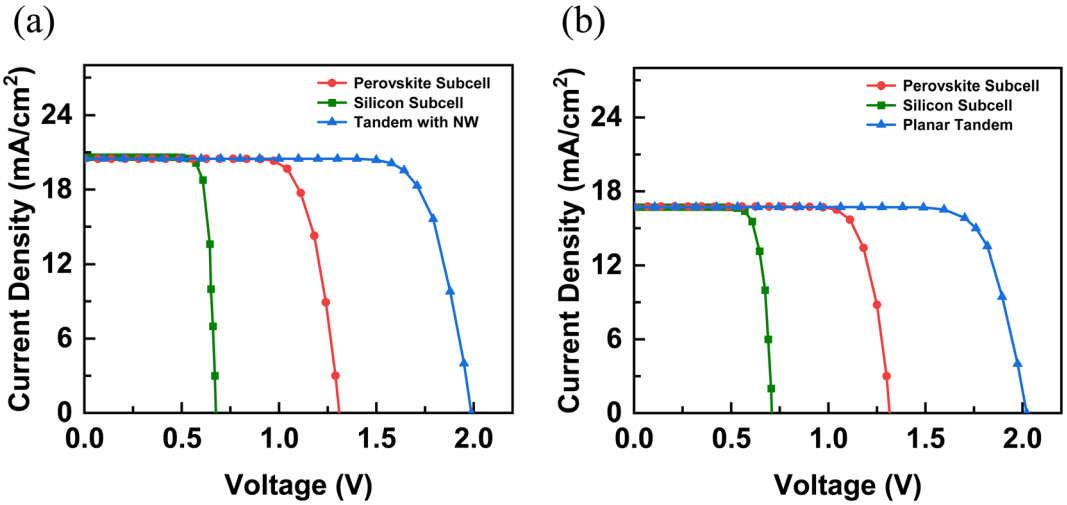

Fig. 8 Calculated J–V characteristics of the (a) perovskite/Si NW tandem, (b) perovskite/Si planar tandem displaying both the individual contributions from the top and bottom subcells as well as the total device performance.

NWs on top. With the Si NWs, on top of the c-Si, the tandem cell exhibits a significantly higher generation rate throughout the depth of bottom Si, particularly near the surface, due to improved light trapping and scattering. The contour plots at $\lambda =$ 811 nm illustrate the electric field profiles inside the c-Si with (Fig. 7(b)) and without the NWs (Fig. 7(c)). The incorporation of NWs results in alternating bright and dark regions, indicating localized field enhancements, which are absent in the planar configuration. The enhanced carrier generation rate and oscillatory pattern in perovskite/Si tandem has been explained in previous studies, by taking into account, the lensing effect of the NWs.[41,42] Lu, *et. al.*[41] reported that NWs, due to their high aspect ratio and waveguiding ability, can form focused dark and bright spots, leading to enhanced photon absorption and carrier generation in certain regions in the bulk.

4.4 Tandem solar cell output characteristics

The 3D carrier generation rates for both the top perovskite and the bottom Si cell are spatially averaged to form a 1D generation profile, which is used by SCAPS-1D to extract the electrical characteristics of the tandem solar cell. The standalone top and bottom subcells are simulated separately and then for the tandem configuration, the subcell currents are matched by adjusting the thickness of the top perovskite as shown in Fig. 8(a) and (b). For c-Si without the NWs, current matching occurs when the thickness of the perovskite is 220 nm. When an array of Si NWs is grown on top, a thicker perovskite (~530 nm) is needed to match the subcell currents. The bulk c-Si thickness is maintained at 180 μm in both configurations. The ITO–Si interface defect density was set to practical values for both planar and Si NW tandem configurations, with 10^{15} cm^{-3} for the Si NW case and 10^{11} cm^{-3} for the planar cell, reflecting the significantly smaller interface area in the latter.[43] Consequently, the higher interface defect density in the Si NW structure resulted in a reduction in V_{OC} relative to its planar counterpart, which can be attributed to enhanced carrier recombination arising from the significantly larger ITO–Si contact area in the NW geometry. Table 1 summarizes the output characteristics of both the current matched tandem solar cells, with and without the NWs. The short-circuit current density (J_{SC}) and PCE of the tandem cell, with the Si NW array on top, are 22.6% and 5.13% higher, respectively, than the corresponding values without the Si NWs. This improvement reflects the nanophotonic effects of the NW architecture, which enhance light absorption and consequently increase electron–hole pair generation within the device.

To benchmark the performance of our proposed design within the current state of the art, we compared the PCE of our device with leading experimentally demonstrated perovskite-Si monolithic tandems reported in the literature. For instance, Chin *et al.* achieved a certified 31.25% efficiency through advanced interface passivation engineering.[16] Ashouri *et al.* reported a 29.15% device enabled by reduced nonradiative recombination at the hole-selective interface,[22] while Pei *et al.* demonstrated a 30.52% tandem using reactive passivation at the perovskite–ETL interface.[44] In comparison, our Si NW-integrated tandem architecture attains a simulated PCE of 32.11%, exceeding the performance of these experimentally realized devices. This comparison, summarized in Fig. 9, underscores the strong potential of incorporating a NW-

Table 1 Output characteristics of the 2-T tandem solar cells

Solar cell	J_{SC} (mA cm^{-2})	V_{OC} (V)	FF (%)	PCE (%)
2-T Perovskite/Si tandem	16.71	2.02	79.91	26.98
2-T Perovskite/Si NW tandem	20.48	1.99	78.79	32.11

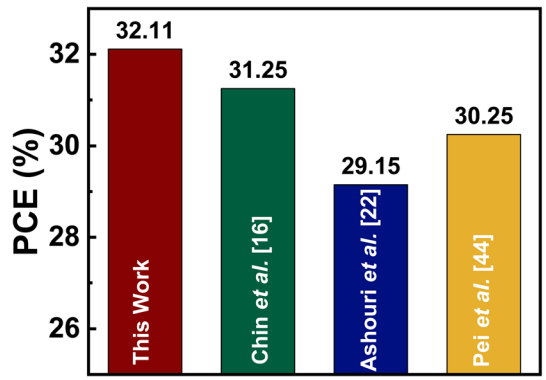

Fig. 9 Comparison between the PCEs of the proposed design with state-of-the-art perovskite/Si tandems reported in literature.

enhanced Si bottom subcell for next-generation monolithic perovskite/Si tandem photovoltaics.

5. Conclusion

In this work, we have proposed a novel 2-T perovskite/c-Si tandem solar cell, where an array of vertically aligned Si NWs is grown on top of the underlying c-Si. The Si NWs, which extend into the interlayer, connects the two subcells and significantly enhances the coupling of incident light from the top perovskite subcell to the bottom c-Si subcell through waveguiding effect and Fabry–Pérot resonance modes. Under current matched conditions, the proposed perovskite/Si tandem has 5.13% higher PCE than conventional perovskite/Si tandem solar cells without the NW array. The PCE can be further enhanced by optimizing the NW material, shape and geometry. This work presents a new insight towards minimizing interlayer losses and achieving highly efficient perovskite/Si tandems.

Author contributions

Conceptualization: T. Rahman and M. Hossain; data curation, formal analysis, investigation, methodology, visualization, writing – original draft: A. Saha and M. A. Fatin; writing – review and editing: T. Rahman and M. Hossain; project administration and supervision: M. Hossain.

Conflicts of interest

The authors declare no conflicts of interest.

Data availability

All data included in this study are available from the corresponding authors upon request. For any specific inquiries, please contact Mainul Hossain E-mail: mainul.eee@du.ac.bd.

Supplementary information (SI): Section S1: Calibration of the simulated top and bottom subcells. Section S2: Optimization of the Si NW geometry for maximum absorption. Section S3: Overall absorption enhancement. Fig S1: Calibrated J–V curves for the standalone subcells under AM1.5G incident light. Fig S2: Results of FDTD simulations with TM polarized incident light showing absorbance spectra (a–c) for different NW radii (r_{NW} = 90 nm, 170 nm, 250 nm) when periodicity (P) is varied, and (d) for different periodicities (P = 600 nm, 700 nm, 800 nm) at the optimum radius (r_{NW} = 250 nm). Table S1: Output parameters of the simulated subcells compared with experimental values. Table S2: Input parameters for simulated perovskite top subcell. Table S3: Input parameters for simulated Si bottom subcell. Table S4: Absorption ratio of Si NWs to bulk Si at selected wavelengths. See DOI: https://doi.org/10.1039/d5ra07413d.

Acknowledgements

T. Rahman gratefully acknowledges support from EPSRC grant EP/X033333/1. All authors thankfully recognize the support from Fab Lab DU, at University of Dhaka, and Bangladesh Research and Education Network (BdREN) for providing the necessary computational resources for this simulation study. The authors also gratefully acknowledge Yeasin Arafat Pritom for his insightful contributions and expert guidance in the Lumerical FDTD simulations.

References

1 S. Tombe, G. Adam, H. Heilbrunner, D. H. Apaydin, C. Ulbricht, N. S. Sariciftci, C. J. Arendse, E. Iwuoha and M. C. Scharber, Optical and electronic properties of mixed halide (X = I, Cl, Br) methylammonium lead perovskite solar cells, *J. Mater. Chem. C*, 2017, **5**(7), 1714–1723.
2 J. Y. Kim, J. W. Lee, H. S. Jung, H. Shin and N. G. Park, High-efficiency perovskite solar cells, *Chem. Rev.*, 2020, **120**(15), 7867–7918.
3 W. Shockley and H. J. Queisser, Detailed balance limit of efficiency of p–n junction solar cells, *J. Appl. Phys.*, 1961, **32**(3), 510–519.
4 F. Sahli, J. Werner, B. A. Kamino, M. Bräuninger, R. Monnard, B. Paviet-Salomon, L. Barraud, L. Ding, J. J. Diaz Leon, D. Sacchetto, G. Cattaneo, M. Despeisse, M. Boccard, S. Nicolay, Q. Jeangros, B. Niesen and C. Ballif, Fully textured monolithic perovskite/silicon tandem solar cells with 25.2% power conversion efficiency, *Nat. Mater.*, 2018, **17**(9), 820–826.
5 M. Jošt, E. Köhnen, A. Al-Ashouri, T. Bertram, Š. Tomšič, A. Magomedov, E. Kasparavicius, T. Kodalle, B. Lipovšek, V. Getautis, R. Schlatmann, C. A. Kaufmann, S. Albrecht and M. Topič, Perovskite/CIGS tandem solar cells: From certified 24.2% toward 30% and beyond, *ACS Energy Lett.*, 2022, **7**(4), 1298–1307.
6 K. Bittkau, T. Kirchartz and U. Rau, Optical design of spectrally selective interlayers for perovskite/silicon heterojunction tandem solar cells, *Opt. Express*, 2018, **26**(18), A750–A760.
7 M. A. Steiner, J. F. Geisz, J. S. Ward, I. Garcia, D. J. Friedman, R. R. King, P. T. Chiu, R. M. France, A. Duda, W. J. Olavarria, M. Young and S. R. Kurtz, Optically enhanced photon

recycling in mechanically stacked multijunction solar cells, *IEEE J. Photovoltaics*, 2016, **6**(1), 358–365.

8 M. T. Borgström, M. H. Magnusson, F. DImroth, G. Siefer, O. Höhn, H. Riel, H. Schmid, S. Wirths, M. Björk, I. Åberg, W. Peijnenburg, M. Vijver, M. Tchernycheva, V. Piazza and L. Samuelson, Towards nanowire tandem junction solar cells on silicon, *IEEE J. Photovoltaics*, 2018, **8**(3), 733–740.

9 Y. Hu, M. Li, J. J. He and R. R. Lapierre, Current matching and efficiency optimization in a two-junction nanowire-on-silicon solar cell, *Nanotechnology*, 2013, **24**(6).

10 S. K. Kim, X. Zhang, D. J. Hill, K. D. Song, J. S. Park, H. G. Park and J. F. Cahoon, Doubling absorption in nanowire solar cells with dielectric shell optical antennas, *Nano Lett.*, 2015, **15**(1), 753–758.

11 N. Tavakoli and E. Alarcon-Llado, Combining 1D and 2D waveguiding in an ultrathin GaAs NW/Si tandem solar cell, *Opt. Express*, 2019, **27**(12), A909–A923.

12 X. Yan, C. Zhang, J. Wang, X. Zhang and X. Ren, A high-efficiency Si nanowire array/perovskite hybrid solar cell, *Nanoscale Res. Lett.*, 2017, **12**(14), 14.

13 I. M. Asuo, D. Banerjee, A. Pignolet, R. Nechache and S. G. Cloutier, Perovskite/silicon-nanowire-based hybrid heterojunctions for fast and broadband photodetectors, *Phys. Status Solidi – Rapid Res. Lett.*, 2021, **15**(4), 1–7.

14 Z. Liu, B. Sun, T. Shi, Z. Tang and G. Liao, Enhanced photovoltaic performance and stability of carbon counter electrode based perovskite solar cells encapsulated by PDMS, *J. Mater. Chem. A*, 2016, **4**(27), 10700–10709.

15 V. V Fedorov, A. Bolshakov, O. Sergaeva, V. Neplokh, D. Markina, M. I. Petrov, R. Grange, M. Timofeeva, S. Bruyere, S. V Makarov and I. S. Mukhin, Gallium phosphide nanowires in a free-standing, flexible, and semitransparent membrane for large-scale infrared-to-visible light conversion, *ACS Nano*, 2020, **14**(8), 10624–10632.

16 X. Y. Chin, D. Turkay, J. A. Steele, S. Tabean, S. Eswara, M. Mensi, P. Fiala, C. M. Wolff, A. Paracchino, K. Artuk, D. Jacobs, Q. Guesnay, F. Sahli, G. Andreatta, M. Boccard, Q. Jeangros and C. Ballif, Interface passivation for 31.25%-efficient perovskite/silicon tandem solar cells, *Science*, 2023, **381**(6653), 59–63.

17 S. Akin, F. Sadegh, S. Turan and S. Sonmezoglu, Inorganic $CuFeO_2$ delafossite nanoparticles as effective hole transport materials for highly efficient and long-term stable perovskite solar cells, *ACS Appl. Mater. Interfaces*, 2019, **11**(48), 45142–45149.

18 S. Akin, Y. Liu, M. I. Dar, S. M. Zakeeruddin, M. Grätzel, S. Turan and S. Sonmezoglu, Hydrothermally processed $CuCrO_2$ nanoparticles as an inorganic hole transporting material for low-cost perovskite solar cells with superior stability, *J. Mater. Chem. A*, 2018, **6**(41), 20327–20337.

19 E. Camizci, I. Dilci, Z. Xiao and S. Sonmezoglu, Defect passivation and crystallization management enabled by thulium dopant as B-site cation for highly stable and efficiency fully inorganic perovskite solar cells with over 17% efficiency, *Chem. Eng. J.*, 2025, **512**, 62314.

20 İ. C. Kaya, R. Ozdemir, H. Usta and S. Sonmezoglu, A dopant-free 2,7-dioctyl[1]benzothieno[3,2-b][1]benzothiophene (C8-BTBT)-based hole transporting layer for highly stable perovskite solar cells with efficiency over 22%, *J. Mater. Chem. A*, 2022, **10**(23), 12464–12472.

21 F. Kong, E. Güzel and S. Sonmezoglu, Hydrophobic 4-(isopropylbenzyl)oxy-substituted metallophthalocyanines as a dopant-free hole selective material for high-performance and moisture-stable perovskite solar cells, *Mater. Today Energy*, 2023, **35**, 101324.

22 A. Al-Ashouri, E. Köhnen, B. Li, A. Magomedov, H. Hempel, P. Caprioglio, J. A. Márquez, A. B. Morales Vilches, E. Kasparavicius, J. A. Smith, N. Phung, D. Menzel, M. Grischek, L. Kegelmann, D. Skroblin, C. Gollwitzer, T. Malinauskas, M. Jošt, G. Matič, B. Rech, R. Schlatmann, M. Topič, L. Korte, A. Abate, B. Stannowski, D. Neher, M. Stolterfoht, T. Unold, V. Getautis and S. Albrecht, Monolithic perovskite/silicon tandem solar cell with >29% efficiency by enhanced hole extraction, *Science*, 2020, **370**(6522), 1300–1309.

23 M. Burgelman, P. Nollet and S. Degrave, Modelling polycrystalline semiconductor solar cells, *Thin Solid Films*, 2000, **361–362**, 527–532.

24 Q. Liang, H. Duan, X. Zhu, X. Chen and X. Xia, Solar thermal absorber based on dielectric filled two-dimensional nickel grating, *Opt. Mater. Express*, 2019, **9**(8), 3193–3203.

25 A. Arjmand and D. McGuire, Complete optoelectronic simulation of patterned silicon solar cells, *Opt. Quantum Electron.*, 2014, **46**(10), 1379–1384.

26 R. A. Puglisi, C. Bongiorno, S. Caccamo, E. Fazio, G. Mannino, F. Neri, S. Scalese, D. Spucches and A. La Magna, Chemical vapor deposition growth of silicon nanowires with diameter smaller than 5 nm, *ACS Omega*, 2019, **4**(19), 17967–17971.

27 T. Hanrath and B. A. Korgel, Supercritical fluid-liquid-solid (SFLS) synthesis of Si and Ge nanowires seeded by colloidal metal nanocrystals, *Adv. Mater.*, 2003, **15**(5), 437–440.

28 F. J. Wendisch, M. Rey, N. Vogel and G. R. Bourret, Large-scale synthesis of highly uniform silicon nanowire arrays using metal-assisted chemical etching, *Chem. Mater.*, 2020, **32**(21), 9425–9434.

29 A. D. Refino, N. Yulianto, I. Syamsu, A. P. Nugroho, N. H. Hawari, A. Syring, E. Kartini, F. Iskandar, T. Voss, A. Sumboja, E. Peiner and H. S. Wasisto, Versatilely tuned vertical silicon nanowire arrays by cryogenic reactive ion etching as a lithium-ion battery anode, *Sci. Rep.*, 2021, **11**, 19779.

30 B. Pal, K. J. Sarkar and P. Banerji, Fabrication and studies on Si/InP core-shell nanowire based solar cell using etched Si nanowire arrays, *Sol. Energy Mater. Sol. Cells*, 2020, **204**, 110217.

31 S. B. Kang, J. H. Kim, M. H. Jeong, A. Sanger, C. U. Kim, C. M. Kim and K. J. Choi, Stretchable and colorless freestanding microwire arrays for transparent solar cells with flexibility, *Light Sci. Appl.*, 2019, **8**, 121.

32 P. P. Nakti, D. Sarker, M. I. Tahmid and A. Zubair, Ultra-broadband near-perfect metamaterial absorber for

photovoltaic applications, *Nanoscale Adv.*, 2023, **5**(24), 6858–6869.

33 E. Garnett and P. Yang, Light trapping in silicon nanowire solar cells, *Nano Lett.*, 2010, **10**(3), 1082–1087.

34 T. Bartschmid, F. J. Wendisch, A. Farhadi and G. R. Bourret, Recent advances in structuring and patterning silicon nanowire arrays for engineering light absorption in three dimensions, *ACS Appl. Energy Mater.*, 2022, **5**(5), 5307–5317.

35 B. Wang and P. W. Leu, Tunable and selective resonant absorption in vertical nanowires, *Opt. Lett.*, 2012, **37**(18), 3756–3758.

36 K. Seo, M. Wober, P. Steinvurzel, E. Schonbrun, Y. Dan, T. Ellenbogen and K. B. Crozier, Multicolored vertical silicon nanowires, *Nano Lett.*, 2011, **11**(4), 1851–1856.

37 L. B. Luo, L. H. Zeng, C. Xie, Y. Q. Yu, F. X. Liang, C. Y. Wu, L. Wang and J. G. Hu, Light trapping and surface plasmon enhanced high-performance NIR photodetector, *Sci. Rep.*, 2014, **4**, 3914.

38 G. Fan, H. Zhu, K. Wang, J. Wei, X. Li, Q. Shu, N. Guo and D. Wu, Graphene/silicon nanowire schottky junction for enhanced light harvesting, *ACS Appl. Mater. Interfaces*, 2011, **3**(3), 721–725.

39 Y. F. Huang, S. Chattopadhyay, Y. J. Jen, C. Y. Peng, T. A. Liu, Y. K. Hsu, C. L. Pan, H. C. Lo, C. H. Hsu, Y. H. Chang, C. S. Lee, K. H. Chen and L. C. Chen, Improved broadband and quasi-omnidirectional anti-reflection properties with biomimetic silicon nanostructures, *Nat. Nanotechnol.*, 2007, **2**(12), 770–774.

40 B. M. Rey, R. Elnathan, R. Ditcovski, K. Geisel, M. Zanini, M. A. Fernandez-Rodriguez, V. V. Naik, A. Frutiger, W. Richtering, T. Ellenbogen, N. H. Voelcker and L. Isa, Fully tunable silicon nanowire arrays fabricated by soft nanoparticle templating, *Nano Lett.*, 2016, **16**(1), 157–163.

41 Y. S. Lu, J. Fernades, H. Liu, and H. Jiang, Fresnel lens based on silicon nanowires, *IEEE International Conference on Micro Electro Mechanical Systems*, San Francisco, CA, USA, 2014, pp. 1175–1178.

42 T. Rahman, M. Navarro-Cía and K. Fobelets, High density micro-pyramids with silicon nanowire array for photovoltaic applications, *Nanotechnology*, 2014, **25**, 485202.

43 J. D. Christesen, X. Zhang, C. W. Pinion, T. A. Celano, C. J. Flynn and J. F. Cahoon, Design principles for photovoltaic devices based on Si nanowires with axial or radial p–n junctions, *Nano Lett.*, 2012, **12**(11), 6024–6029.

44 F. Pei, Q. Wang, Z. Wei, X. Zhuang, X. Cheng, K. Li, Y. Cui, L. Wang, Z. Huang, Z. Zhang, T. Xu, Y. Zhang, X. Wang, H. Zhou, Y. Chen and Q. Chen, Tailoring perovskite/C_{60} interface by reactive passivators for stable tandem solar cells, *Adv. Funct. Mater.*, 2024, **34**(52), 2410737.